OXFORD

Cerebral Cortex, 2024, **34**, bhae471
https://doi.org/10.1093/cercor/bhae471
Advance access publication date 5 December 2024
Original Article

Testing Hubel and Wiesel's "ice-cube" model of functional maps at cellular resolution in macaque V1

Sheng-Hui Zhang[1,2], Shi-Ming Tang[2,3,4,*], Cong Yu[1,4,*]

[1]School of Psychological and Cognitive Sciences, Peking University, 5 Yiheyuan Road, Beijing 100871, China
[2]PKU-Tsinghua Center for Life Sciences, Peking University, 5 Yiheyuan Road, Beijing 100871, China
[3]School of Life Sciences, Peking University, 5 Yiheyuan Road, Beijing 100871, China
[4]IDG-McGovern Institute for Brain Research, Peking University, 5 Yiheyuan Road, Beijing 100871, China
[*]Corresponding authors: Shi-Ming Tang, School of Life Sciences, Peking University, 5 Yiheyuan Road, Beijing 100871, China. Email: tangshm@pku.edu.cn; Cong Yu, School of Psychological and Cognitive Sciences, Peking University, 5 Yiheyuan Road, Beijing 100871, China. Email: yucong@pku.edu.cn

Hubel and Wiesel's ice-cube model proposed that V1 orientation and ocular dominance functional maps intersect orthogonally to optimize wiring efficiency. Here, we revisited this model and additional arrangements at both cellular and pixel levels in awake macaques using two-photon calcium imaging. The recorded response fields of view were similar in size to hypercolumns, each containing up to 2,000 identified neurons and representing full periods of orientation preferences and ocular dominance. We estimated each neuron/pixel's orientation, ocular dominance, and spatial frequency preferences, constructed respective functional maps, computed geometric gradients of feature preferences, and calculated intersection angles among these gradients. At the cellular level, the intersection angles among functional maps were nearly evenly distributed. Nonetheless, pixel-based maps after Gaussian smoothing displayed orientation-ocular dominance and orientation–spatial frequency orthogonality, as well as ocular dominance–spatial frequency parallelism, in alignment with previous results, even though the trends were weak and highly variable. However, these Gaussian smoothing effects were not observed in cellular maps, indicating that the pixel-based trends may not accurately represent the relationships among feature-tuning properties of V1 neurons. We suggest that the widely distributed intersections among cellular maps can ensure that multiple stimulus features are represented within a hypercolumn, and no pair of features is represented with the least economical wiring (e.g. parallel intersections).

Key words: ice-cube model; functional maps; macaque; V1; two-photon imaging.

Introduction

V1 neurons are specialized in processing basic stimulus features, such as orientation, spatial frequency (SF), motion direction, depth, and color. They also have different eye preferences or ocular dominance (OD). Each feature specialization appears to have a distinct functional map, in which neurons tuned to a similar feature dimension (e.g. a specific orientation) are spatially clustered, and the feature tuning of clusters changes smoothly with horizontal displacement (Hubel and Wiesel 1962, 1968; Bartfeld and Grinvald 1992; Weliky et al. 1996; Lu and Roe 2008).

How do different functional maps coexist geometrically? In their seminal "ice-cube" theory, Hubel and Wiesel (1977) hypothesized that for optimal wiring efficiency, the orientation and ocular dominance maps should intersect orthogonally. This hypothesis has found support in subsequent intrinsic-signal optical imaging (ISOI) (Ts'o et al. 1990; Bartfeld and Grinvald 1992) and two-photon imaging studies (Nauhaus et al. 2016), as well as by computational modeling (Swindale 1992; Najafian et al. 2022). Furthermore, ISOI and two-photon imaging studies have also reported orthogonal intersections between the orientation and SF maps (Hübener et al. 1997; Yu et al. 2005; Nauhaus et al. 2012).

However, when considering multiple functional maps, assuming orthogonality among all maps becomes geometrically challenging. To address this difficulty, functional maps have been suggested to intersect orthogonally only in areas where both maps have high gradients (Yu et al. 2005). Alternatively, as orientation–OD maps and orientation-SF maps tend to intersect orthogonally, low and high SF areas may be close to the center or border of OD columns, respectively (Hübener et al. 1997; Nauhaus et al. 2016), so that OD-SF maps tend to be parallel (Nauhaus et al. 2016). Another solution is to treat multiple feature maps as a single map of spatiotemporal energy, which may provide a more accurate description of population activity in V1 (Basole et al. 2003).

The proposed orthogonal or parallel relationships among functional maps are based on pixel-based functional maps primarily derived from ISOI studies. While ISOI has been valuable in identifying large-scale functional patterns in the visual cortex, it presents several technical shortcomings that may affect the accuracy of results. ISOI signals lack cellular information due to low resolution, have a low signal-to-noise ratio (SNR), and are subject to artifacts of blood vessels and Gaussian smoothing. Moreover, changes in light reflectance due to hemodynamic responses can be spatially diffuse, which would lead to a loss of precision in localizing neuronal activity (Das and Gilbert 1995). Consequently, the extent to which the predicted geometric relationships among functional maps accurately reflect the underlying organizational principles of neuronal feature tuning properties in V1 remains fairly uncertain.

In contrast, two-photon imaging technology offers a promising solution to investigate these relationships with higher resolution, even if recent two-photon imaging studies (Nauhaus et al. 2012;

Received: June 18, 2024. **Revised:** November 13, 2024. **Accepted:** November 15, 2024

Nauhaus et al. 2016) studying this topic have primarily relied on pixel-based maps. Our two-photon imaging setup can capture a response field of view (FOV) of 850 × 850 μm^2, roughly corresponding to the size of a V1 hypercolumn, and typically identifies up to 2,000 neurons within each FOV (Li et al. 2017). Our previous imaging results have demonstrated full periods of clustered orientation tuning and OD (Ju et al. 2021; Zhang et al. 2024), suggesting that cellular functional maps may better reveal the true geometric relationships among functional maps. Furthermore, incorporating cellular information is crucial, as our previous results have indicated that cellular SF maps have much narrower SF tuning ranges and weaker SF clustering (Guan et al. 2021) compared to pixel-based SF maps in a study by Nauhaus et al. (2012), despite the fact that both types of maps were constructed with two-photon calcium imaging technology. This disparity thus highlights the importance of a cellular approach in accurately elucidating the relationships among functional maps in V1.

Materials and methods

Monkey preparation

Monkey preparations were identical to those reported in a previous study (Guan et al. 2021; Ju et al. 2021). Five rhesus monkeys (*Macaca mulatta*) aged 4 and 6 years were each prepared with two sequential surgeries under general anesthesia and strictly sterile conditions. In the first surgery, a 20 mm diameter craniotomy was performed on the skull over V1. The dura was opened and multiple tracks of 100 to 150 nl AAV1.hSynap.GCaMP5G.WPRE.SV40 (AV-1-PV2478, titer 2.37e13 [GC/ml], Penn Vector Core) spaced approximately 1 mm apart were pressure-injected at a depth of ~350 μm. Then, the dura was sutured, the skull cap was re-attached with three titanium lugs and six screws, and the scalp was sewn up. After the surgery, the animal was returned to the cage and treated with injectable antibiotics (Ceftriaxone sodium, Youcare Pharmaceutical Group, China) for 1 week. Postoperative analgesia lappaconite hydrobromide was also injected twice a day, 1 ml per injection. The second surgery was performed 45 days later. A T-shaped steel frame was installed for head stabilization, and an optical window was inserted onto the cortical surface. Data collection could start as early as 1 week later. More details of the preparation and surgical procedures can be found in Li et al. (2017). The procedures were approved by the Institutional Animal Care and Use Committee, Peking University.

Behavioral task

After a 10-day recovery from the second surgery, monkeys were seated in primate chairs with head restraints. They were trained to hold fixation on a small white spot (0.1°) with eye positions monitored by an ISCAN ETL-200 infrared eye-tracking system (ISCAN Inc.) at a 120 Hz sampling rate (Monkeys A, C, & D) or an Eyelink-1000 (SR Research) at a 1,000 Hz sampling rate (Monkeys B & E). During the experiment, trials with the eye position deviated 1.5° or more from the fixation before stimulus offset were discarded as ones with saccades and repeated. For the remaining trials, the eye positions were mostly concentrated around the fixation point, with eye positions in over 95% of trials within 0.5° from the fixation point. For example, the eye movements of Monkey B were sampled 1,000 times for each 1,000 ms stimulus presentation per trial. A trial was regarded to have proper fixation when at least 500 samples of eye positions were within a radius of 0.50° from the central fixation. We found that 95.14% of the trials were within a cutoff radius of 0.50°.

Visual stimuli

For Monkeys A, C, and D, visual stimuli were generated using the ViSaGe system (Cambridge Research Systems) and presented on a 21" Sony G520 CRT monitor (refresh rate = 80 Hz, resolution = 1,280 pixel × 960 pixel, pixel size = 0.31 mm × 0.31 mm). Due to the space limit, the viewing distance varied depending on the stimulus spatial frequency (30 cm at 0.25, 0.5, and 1 cpd; 60 cm at 2 cpd; and 120 cm at 4 and 8 cpd). For Monkeys B and E, visual stimuli were generated using Psychotoolbox 3 (Pelli and Zhang 1991) and presented on a 27" Acer XB271HU LCD monitor (refresh rate = 80 Hz native, resolution = 2,560 pixel × 1,440 pixel native, pixel size = 0.23 mm × 0.23 mm). The viewing distance was 50 cm for lower frequencies (0.25, 0.5, and 1 cpd) and 100 cm for higher frequencies (2, 4, and 8 cpd). For both monitors, the screen luminance was linearized by an 8-bit look-up table, and the mean luminance was approximately 47 cd/m^2.

A drifting square-wave grating (SF = 4 cpd, contrast = full, speed = 3 cycles/s, starting phase = 0°, and size = 0.4° in diameter) was first used to determine the location, eccentricity (1.1° to 3.5°) and size (0.8° to 1°) of the population receptive field associated with an FOV, as well as ocular dominance columns when monocularly presented to confirm the V1 location. This fast process used a 4× objective lens mounted on the two-photon microscope and revealed no cell-specific information.

Neuronal responses were measured with a high-contrast (0.9) Gabor grating (Gaussian-windowed sinusoidal grating) drifting at 2 cycles/s in opposite directions perpendicular to the Gabor orientation, which was presented monocularly to either the ipsilateral or the contralateral eye. The starting phase of the drafting Gabors was always 0°. The Gabor grating varied at twelve orientations from 0° to 165° in 15° steps and six SFs from 0.25 to 8 cpd in 1-octave steps.

In addition, three stimulus sizes (with constant stimulus centers) were used at each spatial frequency for two purposes. Firstly, our pilot measurements suggested very strong surround suppression with larger stimuli. Therefore, comparing responses to different stimulus sizes could help approximate the receptive field size of each neuron that produced maximal response and least surround suppression. Secondly, larger stimuli would have better chances of triggering neurons whose RF centers and the stimulus center were misaligned. It is worth noting that for additional neurons whose RFs had less overlap even with the largest stimuli used, they would have weaker and less orientation-tuned responses because of the Gaussian-blurred stimulus edge. These neurons would most likely be filtered out during our multiple steps of selection of orientation-tuned neurons (see below).

Specifically, the stimulus sizes, represented by the σ of the Gaussian envelope of the Gabor, were 0.64λ and 0.85λ at all SFs, and were additionally smaller at 0.42λ when the SFs were 0.25 to 1 cpd and larger at 1.06λ when the SFs were 2 to 8 cpd (λ: wavelength). Gabors at various SFs, if having the same σ in wavelength unit, would have the same number of cycles. Here at the smallest σ (0.42λ), the Gabors still had a sufficient number of cycles (frequency bandwidths = 1 octave) (Graham 1989) so that the actual stimulus spatial frequencies were precise at nominal values. In terms of visual angle, σ = 1.68°, 2.56°, and 3.36° at 0.25 cpd; 0.84°, 1.28°, and 1.68° at 0.5 cpd; 0.42°, 0.64°, and 0.85° at 1 cpd; 0.34°, 0.42°, and 0.53° at 2 cpd; 0.17°, 0.21°, and 0.26° at 4 cpd, and 0.08°, 0.11°, and 0.13° at 8 cpd, respectively.

Each stimulus was presented for 1,000 ms, with an interstimulus interval (ISI) of 1,500 ms sufficient to allow the calcium signals to return to the baseline level (Guan et al. 2020). Each stimulus condition was repeated twelve times with six repeats for

each opposite direction. Recording at a specific viewing distance was completed before moving to the next one, and all stimuli at each relevant distance were pseudo-randomly presented. When a stimulus was presented monocularly to one eye, the other eye was covered with a translucent eye patch, which reduced the impacts of short-term monocular deprivation. During recordings, contralateral and ipsilateral stimulations alternated in blocks of trials, with at least a 10-min break between blocks. During the breaks, the translucent eye mask was off. Each block of trials typically lasted 20 to 25 min.

Two-photon imaging

Two-photon imaging was performed at V1 superficial layers using a Prairie Ultima IV (In Vivo) two-photon microscope (Prairie Technologies) for Monkeys A, C, and D, and a FENTOSmart two-photon microscope (Femtonics) for Monkeys B and E, along with a Ti:sapphire laser (Mai Tai eHP, Spectra Physics). The recording depth was 200 μm for Monkeys A to C, 250 μm for Monkey D, and 210 μm for Monkey E. One FOV measuring 850 × 850 μm^2 was selected in each animal and imaged using a 1,000 nm femtosecond laser under a 16× objective lens (0.8 N.A., Nikon) at a resolution of 1.6 μm/pixel. Fast resonant scanning mode (32 frames per second) was chosen to obtain continuous images of neuronal activity (8 frames per second after averaging every 4 frames). During recording, the strength of fluorescent signals (indicated by the mean luminance of a small area) was monitored and adjusted if necessary to compensate the drift of fluorescent signals.

Imaging data analysis: Initial screening of ROIs

The data were analyzed using customized MATLAB codes. A normalized cross-correlation-based translation algorithm was used to reduce motion artifacts (Li et al. 2017). Then fluorescence changes were associated with corresponding visual stimuli through the time sequence information recorded by the Neural Signal Processor (Cerebus system, Blackrock Microsystem). By subtracting the mean of the four frames before stimuli onset ($F0$) from the average of the sixth–ninth frames after stimuli onset (F) across five or six repeated trials for the same stimulus condition (same orientation, spatial frequency, size, and drifting direction), the differential image ($\Delta F = F - F0$) was obtained.

For a specific FOV, imaging data with ipsilateral and contralateral conditions were combined using a normalized cross-correlation-based translation algorithm on the basis of the same reference images from recordings with the least head movements and highest self-correlations. Then the regions of interest (ROIs) or possible cell bodies were determined through sequential analysis of 432 differential images in the order of spatial frequency (6), size (3), orientation (12), and eye (2) ($6 \times 3 \times 12 \times 2 = 432$). The first differential image was filtered with a band-pass Gaussian filter (size = 2 to 10 pixels), and connected subsets of pixels (>25 pixels, which excluded smaller vertical neuropils) with average pixel value > 3 SD of the mean brightness were selected as ROIs. Then, the areas of these ROIs were set to mean brightness in the next differential image before the bandpass filtering and thresholding were performed. This measure gradually reduced the standard deviations of differential images and facilitated the detection of neurons with relatively low fluorescence responses. If a new ROI and an existing ROI from the previous differential image overlapped, the new ROI would be on its own if the overlapping area (OA) < 1/4 ROI_{new}, discarded if 1/4 ROI_{new} < OA < 3/4 ROI_{new}, and merged with the existing ROI if OA > 3/4 ROI_{new}. The merges would help smooth the contours of the final ROIs. This process was repeated for all 432 differential images twice to select ROIs. Finally, the roundness for each ROI was calculated as:

$$Roundness = \frac{\sqrt{4\pi \times A}}{P}$$

where A was the ROI's area and P was the perimeter. Only ROIs with roundness larger than 0.9, which would exclude horizontal neuropils, were selected for further analysis. The sizes of the ROIs ranged from 3.3 to 19.3 μm in diameter, with an average of 8.9 ± 1.3 μm.

Imaging data analysis: orientation tuning, SF tuning, and ocular dominance

The ratio of fluorescence change ($\Delta F/F0$) was calculated as a neuron's response to a specific stimulus condition. For a specific neuron's response to a specific stimulus condition, the $F0_n$ of the n-th trial was the average of 4 frames before stimulus onset (−500 to 0 ms), and F_n was the average of the fifth to eighth frames after stimulus onset (500 to 1,000 ms). $F0_n$ was then averaged across 12 trials to obtain the baseline $F0$ for all 12 trials (to reduce noises in the calculations of responses), and $\Delta F_n/F0 = (F_n - F0)/F0$ was taken as the neuron's response to this stimulus at the n-th trial. For a small portion of neurons (e.g. 2.1% to 9.8% in Monkeys A to E) showing direction selectivity, as their responses to two opposite directions differed significantly ($P < 0.05$, Friedman test), the six trials at the preferred direction were considered for calculations of $\Delta F_n/F0$ as the neuron's responses to a particular stimulus. $F0$ was still averaged over 12 trials at two opposite directions.

Several steps were then taken to determine whether a neuron was tuned to orientation and/or spatial frequency, and, if so, its ocular dominance index was calculated. For each monocular condition, the orientation, SF, and size (σ) that produced the maximal response among all conditions were selected. Then, responses to the other 11 orientations and 5 SFs were determined at the selected SF and size. Second, to identify orientation and/or SF-tuned neurons, a nonparametric Friedman test was performed to determine whether a neuron's responses at 12 orientations or 6 SFs were significantly different from each other under at least one monocular stimulation. To reduce Type-I errors, the significance level was set at $\alpha = 0.01$. Third, for those showing significant orientation differences, the trial-based orientation responses of each neuron were fitted with a Gaussian model:

$$R(\theta) = a_1 2^{-\left(\frac{\theta-\theta_0}{\sigma}\right)^2} + b$$

where $R(\theta)$ was the response at orientation θ, and the free parameters a_1, θ_0, σ, and b were the amplitude, peak orientation, standard deviation of the Gaussian function, and minimal response of the neuron, respectively. Only neurons with a goodness of fit $R^2 > 0.5$, at least under one monocular stimulation, were finally selected as orientation-tuned neurons (Fig. 1B). The tuned orientation of the neuron was one of two monocular peak orientations that generated a higher response. The amplitude parameter a_1 was positive in all selected orientation neurons. Fourth, for those showing a significant SF difference, the trial-based SF responses of each neuron were further fitted with a difference-of-Gaussian model.

$$R(sf) = a_1 e^{-\left(\frac{sf}{\sigma_1}\right)^2} - a_2 e^{-\left(\frac{sf}{\sigma_2}\right)^2} + b$$

where $R(sf)$ was a neuron's response at spatial frequency sf, the free parameters a_1, σ_1, a_2, and σ_2 were amplitudes and standard

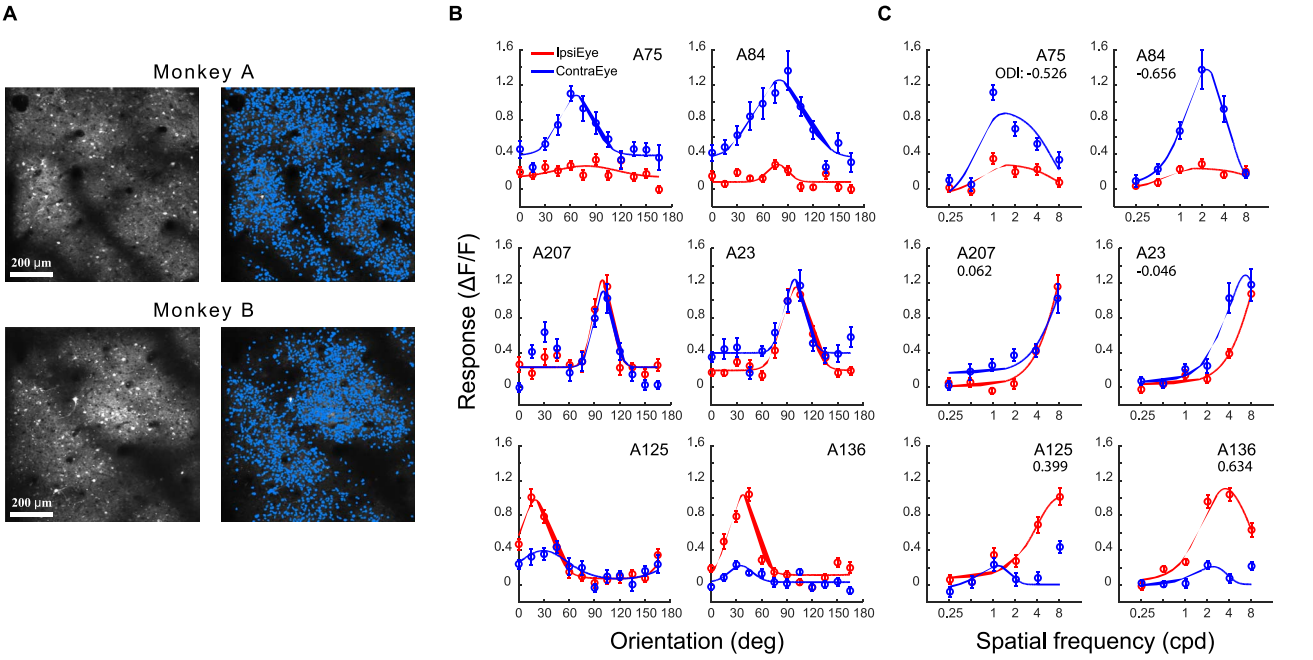

Fig. 1. Two-photon imaging and orientation, spatial frequency, and ocular dominance responses of exemplar neurons. A) Two-photon imaging. Left: Examples of the average 2-photon images over a recording session. Right: Extracted neurons from the exemplar images. B) Orientation responses of six exemplar neurons from Monkey A to stimuli presented in the contralateral and ipsilateral eyes, respectively. The smooth curves are Gaussian fittings. From top to bottom: Neurons preferring the contralateral eye, both eyes, and the ipsilateral eye. C) Spatial frequency responses of the same neurons. The smooth curves are difference-of-Gaussian fittings. Error bars represent ±1 SE. The ODI was calculated and labeled under each neuron's ID number.

deviations of two Gaussians, respectively, and the free parameter b was the minimal response among six spatial frequencies. Only those with a goodness of fit $R^2 > 0.5$, at least under one monocular stimulation, were selected as SF-tuned neurons. The tuned SF of the neuron was one of two monocular peak SFs that generated a higher response. Finally, an ocular dominance index (ODI) was calculated for each selected orientation and/or SF-tuned neurons: $ODI = (R_i - R_c)/(R_i + R_c)$, where R_i was the maximal response to ipsilateral stimulation, and R_c was the maximal response to contralateral stimulation.

Pixel-based data analysis

Pixel-based data analysis was the same as the analysis in Nauhaus et al. (2012). Specifically, the orientation and SF tuning functions of a specific pixel were calculated in the same way as the orientation and SF tuning functions of a specific neuron. The orientation preference was computed as $(1/2)\angle\sum_\theta T_\theta e^{i2\theta}$, where T_θ was the orientation tuning function. The SF preference was determined by first computing the center of mass (CoM) of the SF tuning function in the logarithmic domain, $CoM\left[T_{\log_2(\phi)}\right]$, followed by taking 2^{CoM} to transform the metric into units of cycles/degree. The ODI was calculated as $ODI = (R_i - R_c)/(R_i + R_c)$.

For further analysis, the imaging region was cropped on the basis of an SNR metric. The SNR of each pixel was measured as $(\mu_{max} — \mu_{min})/(SE_{max} + SE_{min})$, where μ_{max} and μ_{min} were the mean responses to the most and least preferred stimuli, and SE_{max} and SE_{min} were the corresponding SEs. Next, this SNR image was smoothened with a 2D Gaussian ($\sigma = 25\ \mu$m). The areas consisting of pixels with SNR > 2 were used for analysis, while areas with SNR < 2 were blackened in the images.

The orientation, OD, and SF maps were further smoothened with a 2D Gaussian ($\sigma = 25\ \mu$m) before their gradient Intersections were calculated.

Cluster index

To quantitatively characterize the clustering of orientation tuning, SF tuning, OD, and intersection angles, we calculated the difference of preferred orientations (ΔPOs), SFs (ΔPSFs), ODIs (ΔODI), and the intersection angle (ΔX_Angle) of each neuron pair as a function of their absolute cortical distance, as well as the corresponding baselines with neuron positions shuffled. The strength of clustering as a function of cortical distance was calculated as the inverse of (ΔPOs_{mean}, $\Delta PSFs_{mean}$, ΔODI_{mean}, or ΔX_Angle_{mean})/Baseline, and the values within the first 50 μm of cortical distance were taken as corresponding cluster indices (CI > 1 when neurons were clustered), respectively.

Gradient intersection

The gradient of a specific neuron/pixel in an orientation map was calculated in the following steps: First, the difference of preferred orientations (Δori) between this neuron/pixel and one of the adjacent neurons/pixels within a radius of 400 μm was calculated as the vector magnitude; second, if Δori < −90°, then Δori = Δori +180°, and if Δori >90°, then Δori = Δori − 180°. The modified Δori represented the vector magnitude, and the vector direction was from this neuron/pixel to the adjacent neuron/pixel. This $\overrightarrow{\Delta ori}$ vector was then normalized by the distance between the two neurons/pixels. Third, the vector sum of all $\overrightarrow{\Delta ori}$ between this neuron/pixel and each adjacent neuron/pixel was obtained as this neuron/pixel's orientation gradient. The OD and SF gradients of a specific neuron/pixel were the vector sums of all $\overrightarrow{\Delta ODI}$ and $\overrightarrow{\Delta \log_2 SF}$ between this neuron/pixel and every other neuron/pixel in the FOV, respectively.

Next, the intersection angle of one neuron/pixel between SF and OD maps was derived from the resultant vector: $\vec{R} = e^{i\times 2\left[Angle\left(\overrightarrow{\Delta ODI}\right) - Angle\left(\overrightarrow{\Delta \log_2 SF}\right)\right]}$. The function *Angle* calculates the angle of gradient, producing values between 0° and 180°. Then,

the intersection angle of one neuron/pixel equals $\left|\frac{1}{2}Angle\left(\vec{R}\right)\right|$, yielding a value between 0° and 90° when $Angle\left(\vec{R}\right)$ is defined within the range of −180° to +180°. Finally, the overall SF-OD intersection angle was determined by the vector sum: $\vec{RO} = \sum_k \vec{R_k}$. The overall SF-OD intersection angle equals $\left|\frac{1}{2}Angle\left(\vec{RO}\right)\right|$, ranges from 0° to 90°. The intersection and overall intersection angle between orientation and SF, along with orientation and OD, were computed in the same manner.

Results

We imaged the responses of V1 superficial-layer neurons to a monocularly (both contralaterally and ipsilaterally) presented Gabor stimulus at various orientations and spatial frequencies in five response FOVs, each from one awake, fixating macaque. The recording depth varied from 200 to 250 μm among FOVs. Each FOV had a size of 850 × 850 μm^2 and was located 1.1° to 3.5° from the central fixation point. Image processing and data analysis identified a total of 9,967 ROIs or possible neurons (Fig. 1A). Among them, 91.2% were tuned to orientation and/or spatial frequency with contralateral and/or ipsilateral stimulus presentations (Friedman test), as exemplified by six neurons in Fig. 1B and C. The ODI of each neuron was calculated as $ODI = (R_i - R_c)/(R_i + R_c)$, where R_i and R_c were the neuron's respective peak responses to ipsilateral and contralateral stimulations. ODI = −1 and 1 would indicate complete contralateral and ipsilateral eye preferences, respectively, and ODI = 0 would indicate equal preferences for both eyes.

Consistent with our earlier report (Ju et al. 2021), the cellular orientation maps displayed significant orientation clustering (Fig. 2A). The cluster indices of the five FOVs ranged from 2.50 to 5.87 (see Materials and Methods for the calculation of cluster indices), with a median cluster index of 3.75 (Fig. 2D). The OD maps (Fig. 2B) also showed clustered neurons, with OD cluster indices ranging from 1.32 to 2.24 and a median of 1.72 (Fig. 2E). The SF maps (Fig. 2C) displayed a limited range of SF tuning, with few neurons tuned to low SFs. Furthermore, SF clustering was weak, with cluster indices ranging from 1.06 to 1.67 and a median of 1.37 (Fig. 2F; a clustering index of 1 indicates zero clustering). These SF results replicate our previous data collected from different macaques with the same procedure (Guan et al. 2021) and are consistent with earlier single-unit results showing an approximately two-octave SF tuning range in V1 neurons (De Valois et al. 1982) and weak or insignificant SF clustering (Edwards et al. 1995; DeAngelis et al. 1999).

To determine the geometric relationships among orientation, OD, and SF maps, we first calculated the respective orientation, OD, and SF gradients for each target neuron in three types of functional maps (Fig. 3A–C). Specifically, we located all neurons within a radius of 400 μm from a target neuron and defined vectors with the target neuron as the coinitial point and these nearby neurons as terminal points. For each pair of target and nearby neurons, the orientation/OD/SF vector magnitudes were the differences of their preferred orientations/ODs/SFs, respectively. We then summed the orientation/OD/SF vectors of all neuron pairs, respectively, with each vector normalized by the distance between the neuron pair, as the target neuron's orientation/OD/SF gradient (see Materials and Methods). The outcomes of gradient computation were largely stable and robust to changes for radii than 150 μm (Fig. 3D).

It is evident that, within the same subarea of a specific FOV, there are often clustered gradient lines along one direction in one gradient map and an orthogonal direction in a different gradient map (e.g. the white-circled region in Ori and OD maps of Monkey A, Fig. 3), or along similar directions in a pair of gradient maps (e.g. the yellow-circled region in Ori and OD maps of Monkey A, Fig. 3). As a result, functional maps exhibit coexisting orthogonal and parallel relationships, as well as other pairings of intersection angles, which are quantified below.

The intersection angles among the orientation, OD, and SF gradients of each neuron were determined by the differences among the directions of these gradients. When necessary, the intersection angles were transformed to be within the range of 0° to 90° (see Materials and Methods, Fig. 4A–C). It is evident that there were no consistent concentrations of intersection angles between ORI and OD maps and between ORI and SF maps (Fig. 4D). Specifically, the intersection angles on average (weighted means) were flat (ORI-OD) or nearly flat with a few % difference between 0° and 90° intersections (ORI-SF) (Fig. 4D). The intersections between SF-OD maps appeared to be parallel more frequently, which was mainly contributed by two FOVs (with 10% more neurons having 0° intersections than 90° intersections), while the other three FOVs showed flatter functions. Additional contour plots were also presented in Supplemental Fig. S1, in which additional data points were added to cellular functional maps using a natural neighbor interpolation method before each map was convolved by a 2D Gaussian ($\sigma = 25$ μm). These plots reveal no significant trends for orthogonal or parallel intersections either.

Together, these cellular maps failed to display a structure in which the OD-ORI and ORI-SF relationships were predominantly orthogonal and the SF-OD relationship was predominantly parallel, as predicted by previous pixel-based functional maps. Furthermore, the intersection angles are clustered (Fig. 4E). This clustering was determined by the gradient maps. For example, when the orientation and OD gradients of neurons in a subarea of an FOV were respectively similar—often caused by similar orientation and OD preferences of these neurons, or by orientation and OD preferences varying at a similar rate—the intersection angles of orientation and OD maps in the same subarea were also similar and clustered.

We refined the analysis in several ways to examine the above outcomes. First, to remove potential measurement errors and cell variances, we divided the 512 pixel × 512 pixel images into grids, each of which was 8 × 8, 16 × 16, or 32 × 32 pixels in size, and averaged the selectivity of neurons within each grid. The patterns of intersection angles did not show any consistent patterns, especially no parallel or orthogonal concentrations, as shown in Supplemental Fig. S2, which displays exemplar maps of feature tunings, gradients, and intersection angles with grids of 32 × 32 pixels. Second, because of the small image size and the blood vessel occlusion, the calculation of the gradient could be inaccurate for neurons close to the edge of the image or to the vessels. We reperformed the calculations after removing these neurons and found basically unchanged results (Supplemental Fig. S3). Third, previously, Yu et al. (2005) reported that the orthogonal relationships were present at locations where the gradients of both the orientation and ocular dominance maps were within the top 30th percentile. However, this trend was not evident in our data either when only the intersection angles of neurons with top 30 percentile gradient values were considered (Supplemental Fig. S4).

Pixel-based functional maps

It is now critical to examine whether our functional maps, if pixel-based, would reveal orthogonal or parallel relationships similar to those from previous studies, particularly from two-photon

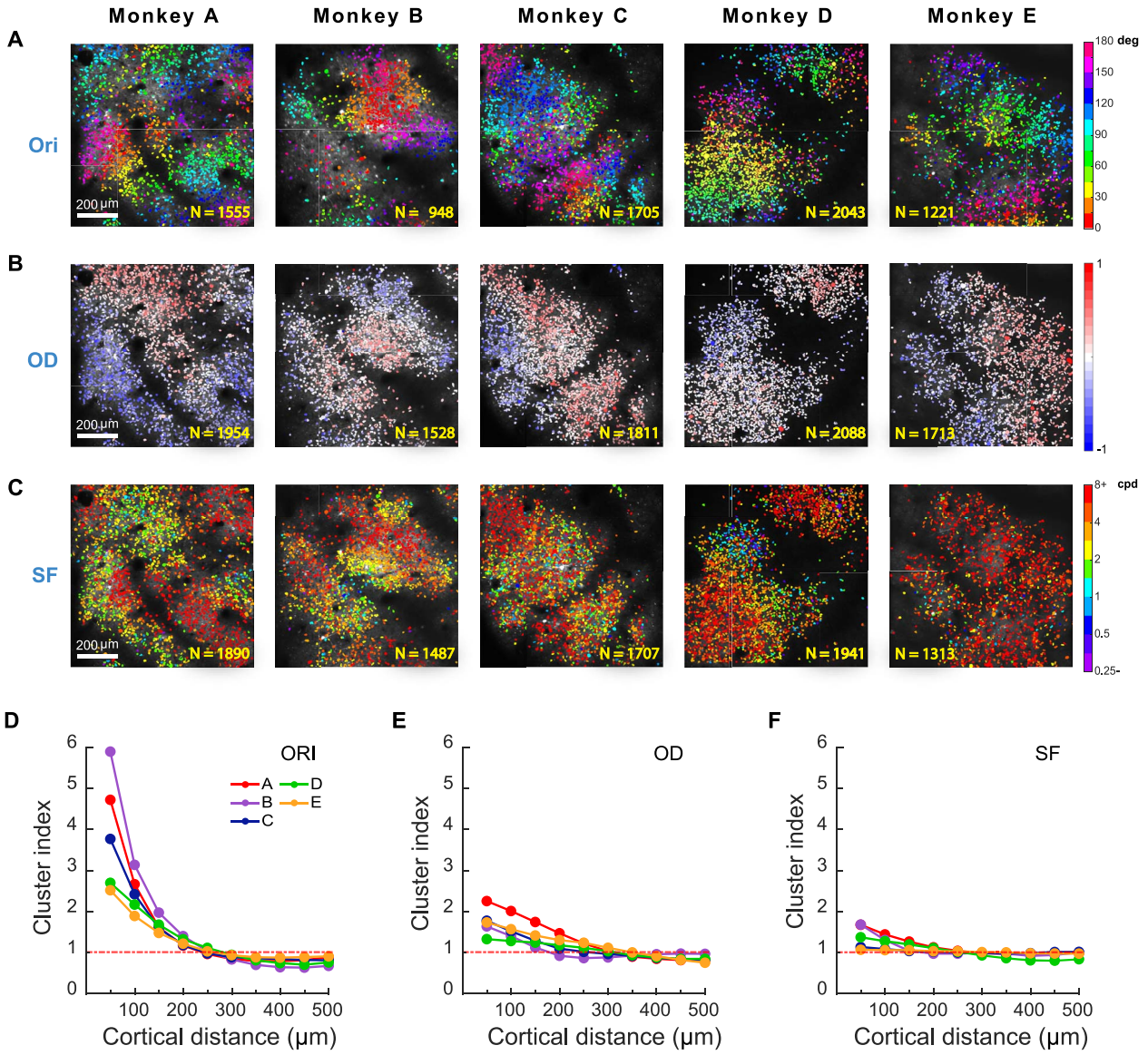

Fig. 2. Functional maps in macaque V1 superficial layers. A–C) Orientation, OD, and SF functional maps with each response FOV. **The peak orientation, OD, and SF preferences of neurons define the values (colors) assigned in their respective parameter maps. All subsequent calculations were based on these maps.** Only neurons with significant orientation, OD, or SF tunings are presented (OD maps of Monkeys C–E were regenerated slightly differently from the same data sets that have been used in a separate paper on binocular combination of monocular inputs; Zhang et al. 2024). D–F) Orientation, OD, and SF clustering. Each datum indicates the average clustering within a 50 μm bin up to the corresponding cortical distance on the x axis. The cluster indices are based on the first 50 μm bin (the leftmost data points).

calcium imaging ones with a similar size of FOVs (Nauhaus et al. 2012; Nauhaus et al. 2016). Following the same procedures in these earlier studies (see Materials and Methods), we calculated each pixel's orientation, OD, and SF preferences for a 512 pixel x 512 pixel image. We then constructed pixel functional maps with Gaussian filtering (σ = 25 μm) and thresholding (Fig. 5A); obtained orientation, OD, and SF gradient information of each pixel (Fig. 5B); and finally, calculated the intersection angles among maps (Fig. 5C). As summarized in Fig. 5D, slight trends of orthogonal (Ori-OD & SF-OD) or parallel (Ori-SF) intersections among maps were evident in some FOVs.

When all the intersection values of all pixels from 5 FOVs were pooled together to simulate the large FOVs in ISOI studies, the overall Ori-OD, SF-OD, and Ori-SF intersections (vector sums) were 87.63°, 61.71°, and 20.41°, respectively, at a Gaussian σ of 25 μm. However, the respective circular variances were very high (0.93, 0.94, and 0.84; a value of 1 indicates a completely even distribution), suggesting wide dispersions of vector values. These outcomes were largely stable for $\sigma \geq 15$ μm (Fig. 6A) and were largely consistent with previous pixel-based ISOI and two-photon imaging results (Hübener et al. 1997; Nauhaus et al. 2016) in terms of vector sums. Nevertheless, the high circular variances indicate that the near orthogonal or parallel intersections among maps, even if genuine, are highly variable. As for cellular functional maps, their geometric relationships after Gaussian smoothing varied greatly among individual FOVs (Fig. 6B), suggesting that the observed trends of Gaussian smoothing in pixel-based functional maps may not be directly related to cellular data.

Discussion

Our results fail to reveal a significant orthogonal relationship between orientation and OD functional maps at the cellular level,

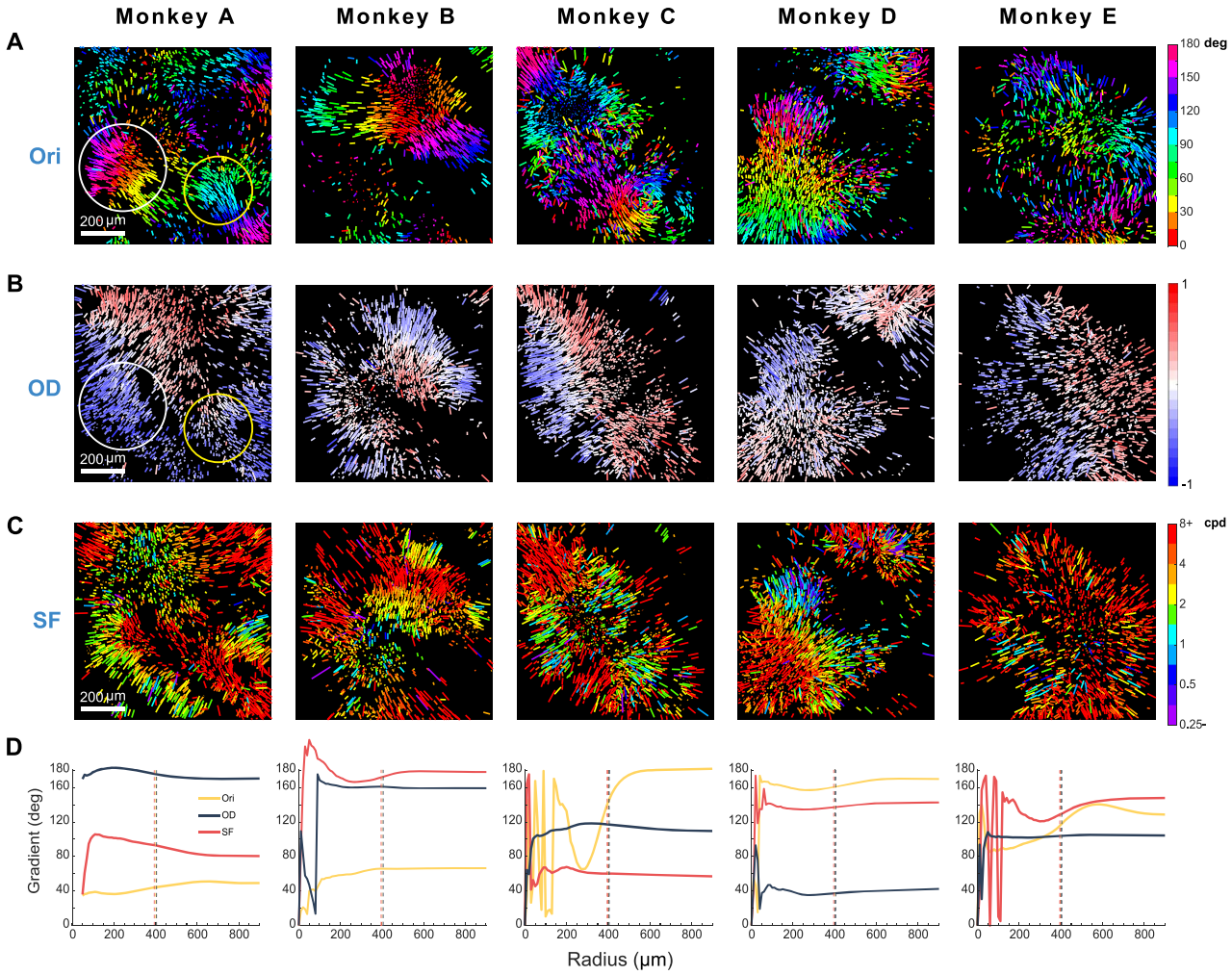

Fig. 3. Orientation, ocular dominance, and spatial frequency gradient maps. A) Orientation gradient maps. Each neuron's gradient, which reflects the sum of respective distance-weighted vectors from it to all neurons within a radius of 400 μm, is represented by a vector bar. The bar length is normalized by the median length of all vector bars within the same FOV and indicates the vector magnitude. B, C) Ocular dominance and spatial frequency gradient maps. Each neuron's ocular dominance or spatial frequency gradient was calculated in the same way. The circles highlight subareas where the gradient lines have orthogonal and parallel relationships between the orientation and ocular dominance maps, respectively. D) The orientation, OD, and SF gradients (the sum of all respective vectors) as a function of the radius of the covered area for gradient calculation.

as would be predicted by the ice-cube model. Additionally, there is no significant evidence for orthogonal intersections between cellular orientation and SF maps, and there is a weak tendency toward parallelism between OD and SF maps in some but not all FOVs (Fig. 4). The pixel-based function maps, on the other hand, suggest the presence of weak and highly variable trends of global orthogonal or parallel relationships among orientation, OD, and SF functional maps as a result of Gaussian smoothing (Fig. 5). These weak trends may have been picked up by previous pixel-based optical imaging studies that cover larger FOVs (Fig. 6), especially when conclusions are drawn without considering high variations, which is typical in ISOI studies. Since no consistent effects of Gaussian smoothing are observed at the cellular level, the pixel-based results may not necessarily reflect the true relationships among the tuning properties of neurons.

The ice-cube model assumes orthogonality between orientation and OD functional maps for efficient neuronal wiring. However, such orthogonal distributions of intersection angles are unattainable among multiple functional maps. Thus, the widely distributed intersection angles may represent a useful compromise, ensuring that no pair of stimulus features is represented by neurons with the least economic wiring (e.g. parallel intersections between maps). In particular, if OD and SF maps were parallel, an area multiple times the size of a hypercolumn would be necessary to fully represent both features. Instead, the current arrangements allow V1 neurons in an area as small as a hypercolumn to completely represent multiple stimulus features, including additional features such as motion direction and disparity with no additional and conflicting requirements for orthogonal or parallel relationships among functional maps.

The clustering of intersection angles appears to be a result of tuning clusters in functional maps. With horizontal displacement, clustered neurons change their stimulus preferences smoothly, leading to similar gradients of tuning changes. When this happens in the same subarea of two or three functional maps, the gradients in each map within this subarea are similar, and their intersections among maps are thus also similar, forming clusters of intersection angles. Whether this clustering of intersection angles represents any functional advantages is unclear, as is the

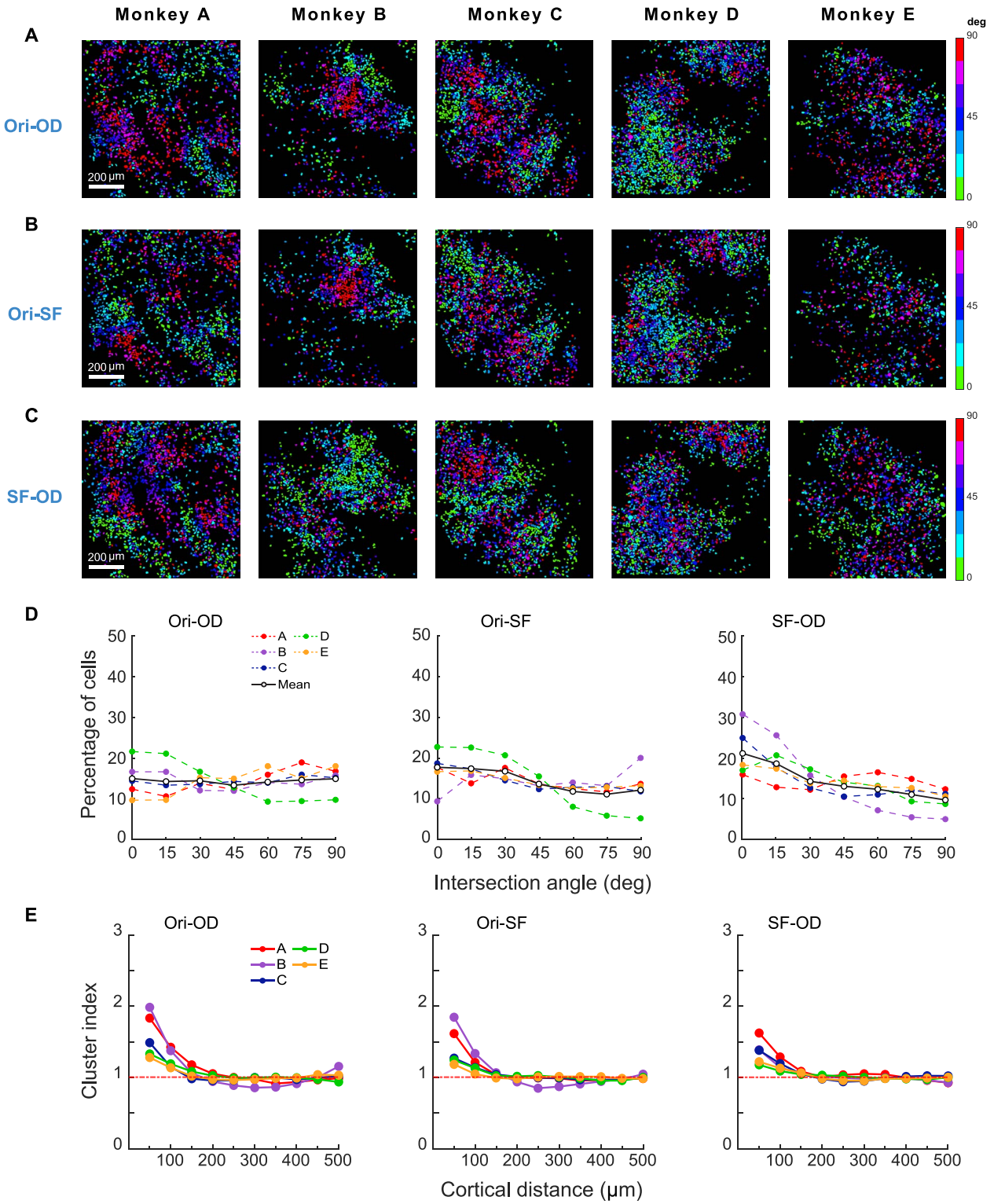

Fig. 4. Geometric relationships among functional maps at cellular resolution. A–C) Maps of intersection angles. From top to bottom: orientation-OD map, orientation-SF map, and SF-OD map, respectively. Intersection angles were mapped from 0° to 90°. D) Distributions of intersection angles. From left to right, orientation-OD map, orientation-SF map, and SF-OD map, respectively. E) Clustering of intersection angles among maps as a function of the cortical distance.

original neuronal clustering in functional maps that eventually determines the clustering of intersection angles. V1 neurons in some animals are orientation selective but not spatially clustered in terms of their orientation tuning, which prompted some researchers to conclude that neural clustering may not serve specific functions (Horton and Adams 2005).

The SF maps in five macaques show limited tuning ranges of medium and high spatial frequencies. Is it possible that SF and OD

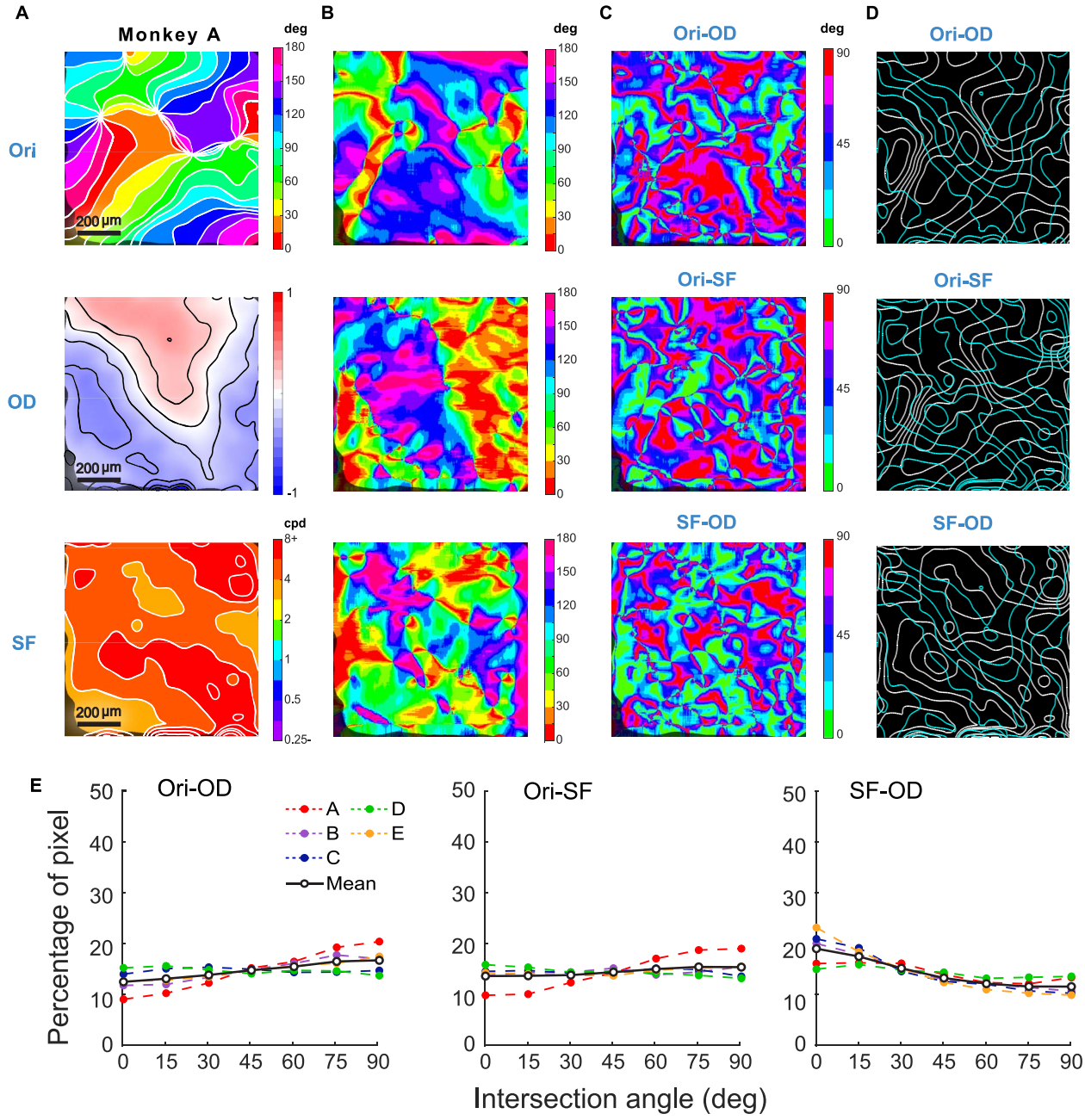

Fig. 5. Pixel-based functional maps. A, B) Pixel-based Gaussian-smoothened orientation (top), OD (middle), and SF (bottom) functional maps A) and gradient maps B) of Monkey A. C) The intersection maps of Monkey A. Top: The Ori-OD intersection map; middle: The Ori-SF intersection map; bottom: The SF-OD intersection map. D) The intersection maps of Monkey A plotted in contour lines. Plots for additional FOVs are presented in Supplemental Fig. S5. E) Distributions of intersection angles in three types of intersection maps for all monkeys.

maps are actually parallel, as suggested by Nauhaus et al. (2016), but we missed areas representing low spatial frequencies because of limited FOV sampling? The medium and high SF presentations have been consistently found in six additional macaques in a previous study of ours using the same two-photon imaging technology and procedures, including cases where neighboring FOVs are imaged (Guan et al. 2021). Considering the sheer number (15) of recorded FOVs, the chance of such strong sampling biases is not very likely.

A technical note: The exact RF size of each ROI was not measured in this study. Nonetheless, it is most likely that the identified neurons had their RFs overlapping with the stimulus, leading to significant responses. A recent study using two-photon imaging (Nauhaus et al. 2016) indicated that the RF scatter in V1 is about half of the original estimate by Hubel and Wiesel (1974). Our own extensive RF mapping data in one macaque not involved in the current study also indicated that the RF scatters of superficial-layer V1 neurons are very narrow (both vertical and horizontal standard deviations are <0.15°) (Supplemental Fig. S6). Therefore, it's likely that our measurements encompassed most neurons that could respond to the stimuli. Some neurons may not have aligned well with the stimulus, resulting in weak and orientation-unspecific responses. These neurons would have been excluded during data analysis (see Materials and Methods).

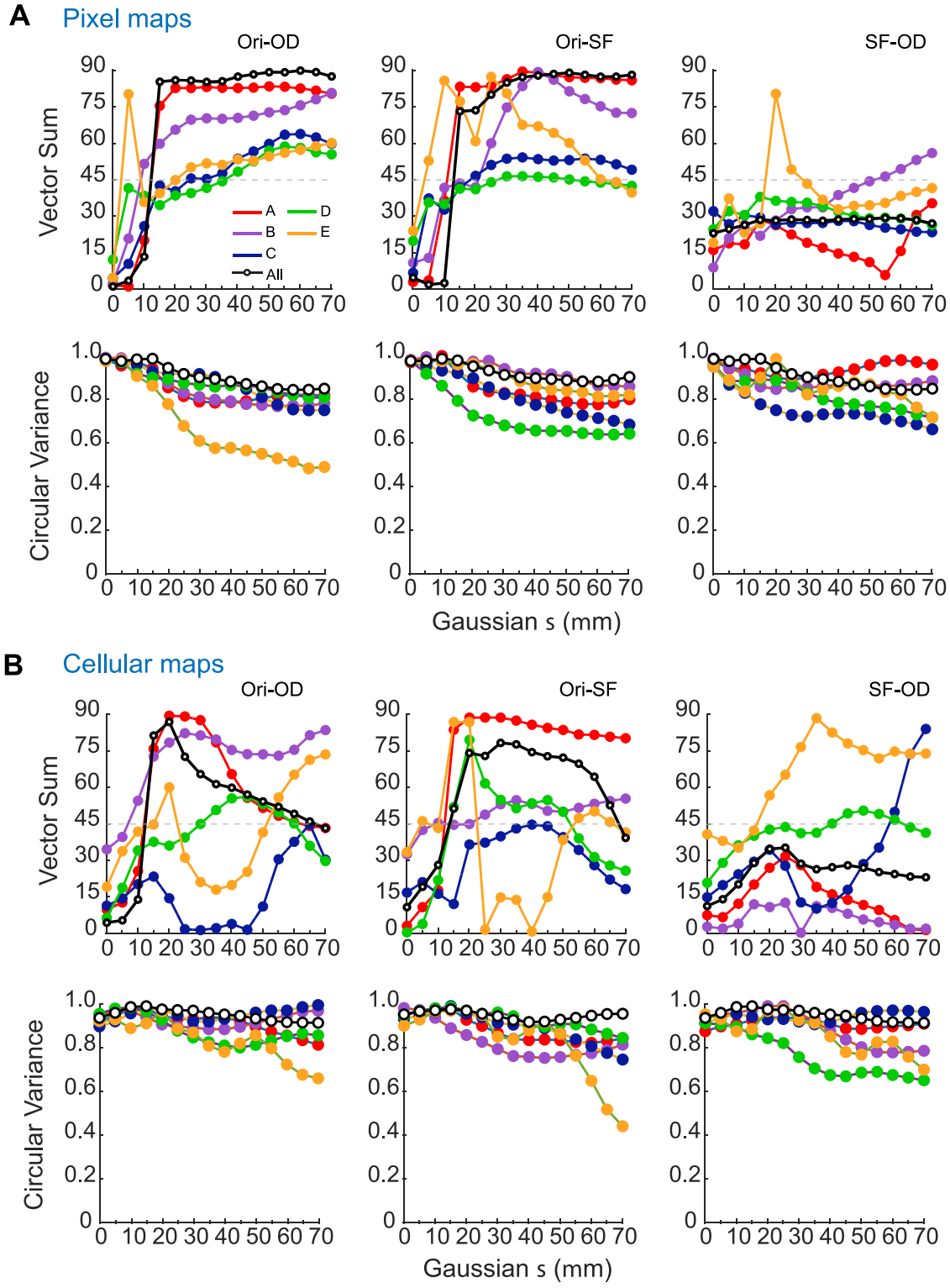

Fig. 6. The effects of Gaussian smoothing on geometric relationships among functional maps. A) Pixel-based functional maps. The upper panels show the intersection angles (vector sums) among maps in individual FOVs and the combined results. The lower panels show corresponding circular variance values. B) Cellular functional maps. Again, the upper panels display the intersection angles (vector sums) among maps in individual FOVs and the combined results, and the lower panels display corresponding circular variance values.

Author contributions

Sheng-Hui Zhang (Data curation, Formal analysis, Writing—original draft), Shi-Ming Tang (Methodology, Writing—review & editing), and Cong Yu (Conceptualization, Formal analysis, Writing—review & editing).

Supplementary material

Supplementary material is available at *Cerebral Cortex* online.

Funding

This study was supported by a STI2030-Major Projects grant (2022ZD0204600), Natural Science Foundation of China grants (31230030 and 31730109), and funds from Peking-Tsinghua Center for Life Sciences, Peking University.

Conflict of interest statement: None declared.

References

Bartfeld E, Grinvald A. Relationships between orientation-preference pinwheels, cytochrome oxidase blobs, and ocular-dominance columns in primate striate cortex. *Proc Natl Acad Sci USA*. 1992:89:11905–11909. https://doi.org/10.1073/pnas.89.24.11905.

Basole A, White LE, Fitzpatrick D. Mapping multiple features in the population response of visual cortex. *Nature*. 2003:423:986–990. https://doi.org/10.1038/nature01721.

Das A, Gilbert CD. Long-range horizontal connections and their role in cortical reorganization revealed by optical recording of cat primary visual cortex. *Nature*. 1995:375:780–784. https://doi.org/10.1038/375780a0.

De Valois RL, Albrecht DG, Thorell LG. Spatial frequency selectivity of cells in macaque visual cortex. *Vis Res*. 1982:22:545–559. https://doi.org/10.1016/0042-6989(82)90113-4.

DeAngelis GC, Ghose GM, Ohzawa I, Freeman RD. Functional micro-organization of primary visual cortex: receptive field analysis of nearby neurons. *J Neurosci*. 1999:19:4046–4064. https://doi.org/10.1523/JNEUROSCI.19-10-04046.1999.

Edwards DP, Purpura KP, Kaplan E. Contrast sensitivity and spatial frequency response of primate cortical neurons in and around the cytochrome oxidase blobs. *Vis Res*. 1995:35:1501–1523. https://doi.org/10.1016/0042-6989(94)00253-I.

Graham N. 1989. *Visual pattern Analyzers (Oxford psychology series, No. 16)*. New York: Oxford University Press, https://doi.org/10.1093/acprof:oso/9780195051544.001.0001.

Guan SC, Zhang SH, Zhang YC, Tang S, Yu C. Plaid detectors in macaque V1 revealed by two-photon calcium imaging. *Curr Biol*. 2020:30:934–940.e3. https://doi.org/10.1016/j.cub.2020.01.005.

Guan SC, Ju N, Tao L, Tang SM, Yu C. Functional organization of spatial frequency tuning in macaque V1 revealed with two-photon calcium imaging. *Prog Neurobiol*. 2021:205:102120. https://doi.org/10.1016/j.pneurobio.2021.102120.

Horton JC, Adams DL. The cortical column: a structure without a function. *Philos Trans R Soc Lond Ser B Biol Sci*. 2005:360:837–862. https://doi.org/10.1098/rstb.2005.1623.

Hubel DH, Wiesel TN. Receptive fields, binocular interaction and functional architecture in the cat's visual cortex. *J Physiol*. 1962:160:106–154. https://doi.org/10.1113/jphysiol.1962.sp006837.

Hubel DH, Wiesel TN. Receptive fields and functional architecture of monkey striate cortex. *J Physiol*. 1968:195:215–243. https://doi.org/10.1113/jphysiol.1968.sp008455.

Hubel DH, Wiesel TN. Uniformity of monkey striate cortex: a parallel relationship between field size, scatter, and magnification factor. *J Comp Neurol*. 1974:158:295–305. https://doi.org/10.1002/cne.901580305.

Hubel DH, Wiesel TN. Ferrier lecture. Functional architecture of macaque monkey visual cortex. *Proc R Soc Lond B Biol Sci*. 1977:198:1–59.

Hübener M, Shoham D, Grinvald A, Bonhoeffer T. Spatial relationships among three columnar systems in cat area 17. *J Neurosci*. 1997:17:9270–9284. https://doi.org/10.1523/JNEUROSCI.17-23-09270.1997.

Ju NS, Guan SC, Tao L, Tang SM, Yu C. Orientation tuning and end-stopping in macaque V1 studied with two-photon calcium imaging. *Cereb Cortex*. 2021:31:2085–2097. https://doi.org/10.1093/cercor/bhaa346.

Li M, Liu F, Jiang H, Lee TS, Tang S. Long-term two-photon imaging in awake macaque monkey. *Neuron*. 2017:93:1049–1057.e3. https://doi.org/10.1016/j.neuron.2017.01.027.

Lu HD, Roe AW. Functional organization of color domains in V1 and V2 of macaque monkey revealed by optical imaging. *Cereb Cortex*. 2008:18:516–533. https://doi.org/10.1093/cercor/bhm081.

Najafian S, Koch E, Teh KL, Jin J, Rahimi-Nasrabadi H, Zaidi Q, Kremkow J, Alonso JM. A theory of cortical map formation in the visual brain. *Nat Commun*. 2022:13:2303. https://doi.org/10.1038/s41467-022-29433-y.

Nauhaus I, Nielsen KJ, Disney AA, Callaway EM. Orthogonal micro-organization of orientation and spatial frequency in primate primary visual cortex. *Nat Neurosci*. 2012:15:1683–1690. https://doi.org/10.1038/nn.3255.

Nauhaus I, Nielsen KJ, Callaway EM. Efficient receptive field tiling in primate V1. *Neuron*. 2016:91:893–904. https://doi.org/10.1016/j.neuron.2016.07.015.

Pelli DG, Zhang L. Accurate control of contrast on microcomputer displays. *Vis Res*. 1991:31:1337–1350. https://doi.org/10.1016/0042-6989(91)90055-A.

Swindale NV. Elastic nets, travelling salesmen and cortical maps. *Curr Biol*. 1992:2:429–431. https://doi.org/10.1016/0960-9822(92)90326-6.

Ts'o DY, Frostig RD, Lieke EE, Grinvald A. Functional organization of primate visual cortex revealed by high resolution optical imaging. *Science*. 1990:249:417–420. https://doi.org/10.1126/science.2165630.

Weliky M, Bosking WH, Fitzpatrick D. A systematic map of direction preference in primary visual cortex. *Nature*. 1996:379:725–728. https://doi.org/10.1038/379725a0.

Yu H, Farley BJ, Jin DZ, Sur M. The coordinated mapping of visual space and response features in visual cortex. *Neuron*. 2005:47:267–280. https://doi.org/10.1016/j.neuron.2005.06.011.

Zhang SH, Zhao XN, Jiang DQ, Tang SM, Yu C. Ocular dominance-dependent binocular combination of monocular neuronal responses in macaque V1. *elife*. 2024:13. https://doi.org/10.7554/eLife.92839.